Chemical Science

ROYAL SOCIETY OF CHEMISTRY

EDGE ARTICLE

View Article Online
View Journal | View Issue

Cite this: *Chem. Sci.*, 2026, **17**, 8242

All publication charges for this article have been paid for by the Royal Society of Chemistry

Targeted reactant activation and spatial charge separation for efficient photocatalytic C(sp^3)–H bond oxidation

Taoran Chen,†[ab] Yu Han,†[ab] Ying Tao,[ab] Guojin Huang,[ab] Zhengwu Liao,[ab] Yulin Wang,[ab] Yue Zheng,[ab] Yu Wang,[ab] Shiqi Li,[c] Wei Zhao,[c] Hongli Sun *[ab] and Chenliang Su [ab]

Received 10th December 2025
Accepted 2nd March 2026

DOI: 10.1039/d5sc09692h

rsc.li/chemical-science

Semiconductor-based photo-redox catalysis offers a sustainable route for green organic synthesis, yet efficient C(sp^3)–H bond oxidation remains challenging due to slow charge separation and limited surface reactivity. Here, we report a CsPCN (cesium doped polymeric carbon nitride)–$Cs_3Bi_2Br_9$ heterojunction that promotes efficient charge separation while retaining strong hole oxidation capability of $Cs_3Bi_2Br_9$ and superior oxygen and reactant activation ability of CsPCN. *In situ* experimental and theoretical studies confirm the photoelectron transfer pathway from $Cs_3Bi_2Br_9$ to CsPCN driven by the interfacial electric field, empowering efficient spatial charge separation and high affinity and activation capability toward oxygen and reactants. As a result, the heterojunction exhibits efficient C(sp^3)–H bond oxidation performance and broad substrate applicability under visible-light irradiation, achieving a conversion rate of ethylbenzene to acetophenone up to 8420 μmol g^{-1} h^{-1}, 4.3 times higher than blank $Cs_3Bi_2Br_9$ (1950 μmol g^{-1} h^{-1}). This work demonstrates a rational heterostructure design strategy to couple charge separation with surface reactant activation for efficient lead-free perovskite based photocatalytic C(sp^3)–H functionalization.

1 Introduction

The selective activation of C(sp^3)–H bonds in aromatic hydrocarbons to produce high-value chemicals has attracted increasing attention due to their broad industrial applications. For example, the oxidation of toluene to benzaldehyde and ethylbenzene to acetophenone provides key intermediates for polystyrene, dyes, pharmaceuticals, and fine chemicals. However, traditional C(sp^3)–H functionalization typically requires strong oxidants or harsh conditions, leading to high energy consumption, undesirable side reactions, and environmental concerns.[1–5] Developing green and sustainable strategies for C(sp^3)–H bond activation is therefore of both scientific and practical significance. Photocatalysis, which utilizes solar energy to drive reactions under ambient conditions, has emerged as a promising alternative for selective hydrocarbon functionalization.

Metal halide perovskites have recently gained considerable attention in solar cells, LEDs, and photocatalysis because of their outstanding optoelectronic properties, including suitable bandgaps, high absorption coefficients, and excellent charge-carrier transport.[6–10] Despite these advantages, their practical photocatalytic C(sp^3)–H bond activation efficiency is often hampered by the severe recombination of the charge carriers and the limited interfacial interaction with hydrocarbon molecules. Constructing heterostructures is a promising and effective strategy to overcome this bottleneck, as heterojunctions can not only prolong lifetime of photogenerated charges, retain strong redox capability of each component, but also significantly enhance surface adsorption and activation of oxygen and reactant molecules, thereby accelerating oxidative reactions.[11–13]

Owing to tunable electronic structure and abundant sites for substrate adsorption and mass transport, alkali-metals doped polymeric carbon nitride (PCN) was selected as a suitable component to construct heterostructures with metal halide perovskites.[14–16] The introduction of alkali-metals into the PCN matrix can further modulate the electronic environment, promote faster charge migration and reduce recombination losses, ultimately boosting the photocatalytic activity toward organic molecular transformations.[17–19]

Herein, we report a CsPCN (cesium doped polymeric carbon nitride)–$Cs_3Bi_2Br_9$ heterojunction photocatalyst that integrates the advantages of promoted carrier transfer and efficient reactant activation in both components. Experimental and theoretical investigations reveal the presence of interfacial electric field directed from CsPCN to $Cs_3Bi_2Br_9$, leading to the

[a]*International Collaboration Laboratory of 2D Materials for Optoelectronics Science and Technology of Ministry of Education, Institute of Microscale Optoelectronics, Shenzhen University, Shenzhen 518060, China. E-mail: hlsun@szu.edu.cn*

[b]*State Key Laboratory of Radio Frequency Heterogeneous Integration, Shenzhen University, Shenzhen 518060, China*

[c]*Institute for Advanced Study, Shenzhen University, Shenzhen, 518060, China*

† Co-first authors.

photogenerated electrons of $Cs_3Bi_2Br_9$ transfer from the conduction band of $Cs_3Bi_2Br_9$ to valence band of CsPCN and recombine the holes there. Such heterojunction not only promotes efficient charge separation but also retains strong hole oxidation capability of $Cs_3Bi_2Br_9$ and the superior oxygen and reactant adsorption ability of CsPCN. Thus, under visible-light irradiation, the heterojunction efficiently oxidizes ethylbenzene to acetophenone and enables the selective conversion of C(sp^3)–H bond of various substrates. This work demonstrates a rational heterostructure design strategy that synergizes reactant activation and charge transfer, offering a general approach to tailor the lead-free perovskite-based photocatalysts for C(sp^3)–H functionalization.

2 Results and discussion

The synthesis process of CsPCN–$Cs_3Bi_2Br_9$ composite (CsPCN–CBB) is presented in Fig. 1a, where the CsPCN was first synthesized by a normal thermal polymerization method with the addition of a certain quantity of CsCl, then introduced into the CBB precursor solution to form the composite by an anti-solvent way.[20,21] The crystal structures of the obtained samples were determined by powder X-ray diffraction (XRD) as shown in Fig. 1b. The peaks at 12.8°, 15.9°, 22.4°, 27.6° and 31.8° were assigned to the (100), (101), (102), (003) and (202) crystal planes of the trigonal CBB (PDF 70-0493), respectively. Note that no peaks of CsPCN were observed in the CsPCN–CBB, due to its amorphous structure and relatively low content. The CsPCN–CBB still maintained trigonal structure, demonstrating that the formation of heterostructure did not change its own structure. Subsequently, the Fourier-transform infrared (FT-IR) spectra of different samples were tested to analyze the chemical structure. As displayed in Fig. 1c, the characteristic peak located at 819 cm^{-1} was assigned to the breathing vibration of triazine units, and the broad peaks between 1200 and 1600 cm^{-1} were attributed to the stretching vibrations of the heterocycle in

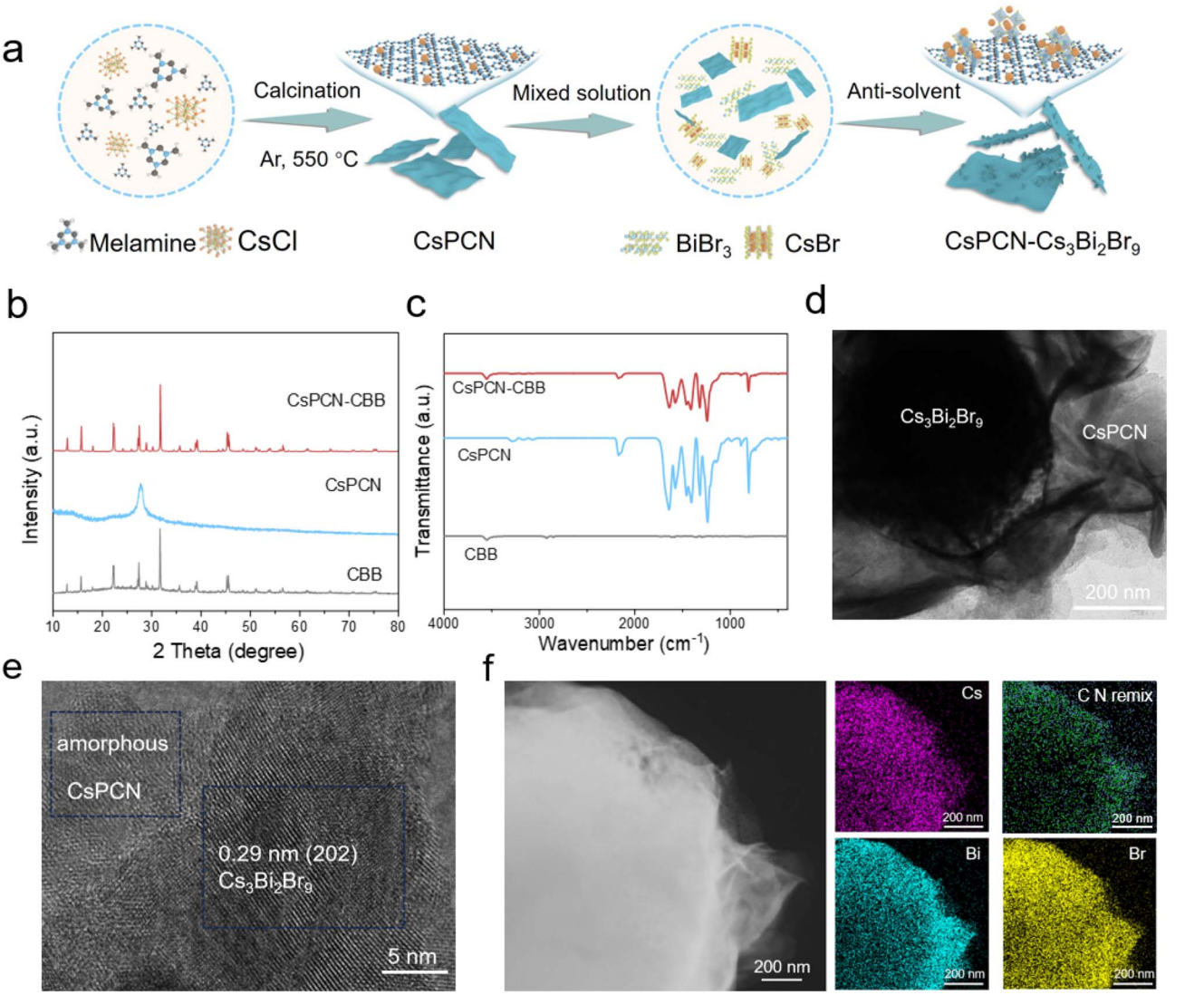

Fig. 1 (a) Schematic for the synthesis of CsPCN–CBB composite. (b) XRD patterns of different composites. (c) FT-IR spectra of different composites. (d) TEM, (e) HRTEM and (f) elemental mapping images of CsPCN–CBB composite.

CsPCN. Two obvious adsorption bands at 962–1128 cm^{-1} and 2086–3047 cm^{-1} in the spectrum of blank CBB also appeared in the spectra of all CsPCN–CBB composites, indicating the successful formation of CsPCN–CBB composite.[22–26] The characterizations of transmission electron microscopy (TEM) have further manifested the successful synthesis of CsPCN–CBB composites. As shown in Fig. 1d, e and S1, the CsPCN exhibited sheet-like morphologies, and the enlarged TEM image of the CsPCN–CBB composite showed an intimate interfacial contact between the CsPCN sheets and the CBB particles. From high-resolution transmission electron microscopy (HRTEM) images, it could be clearly seen that the CBB was wrapped by the CsPCN sheets, and the lattice spacing of 0.29 nm belonging to (202) plane of CBB could be identified.[27,28] The lattice fringes of CsPCN were not observed due to its poor crystalline structure. Moreover, the uniform presence of Cs, Bi, Br, C and N elements in the composites as shown in elemental mapping further confirmed the successful formation of CsPCN–CBB heterostructure (Fig. 1f), consistent with the above analyses. Then the optical absorption properties of three samples were studied by UV-Vis diffuse reflectance spectroscopy (Fig. S2 and S3). The absorption edges of blank CsPCN and CBB were located at 460 and 477 nm respectively, corresponding to the bandgap energies of 2.7 and 2.6 eV using the Kubelka–Munk method, which were consistent with the previous literatures.[29] To further determine the valence band potentials, valence band XPS (VB-XPS) tests were performed to determine the valence-band potentials (E_{VB}) of the samples. According to the equation E_{VB} (*vs.* NHE) = ϕ + $E_{VB,XPS}$ − 4.44 eV, the VB edge potential is converted to the potential relative to the normalized hydrogen electrode (NHE), where the ϕ is the work function of the instrument, and the value is 4.2 eV. Therefore, the VB positions of CBB and CsPCN were calculated to be 1.97 eV and 1.76 eV *vs.* NHE, respectively (Fig. S4). In combination with bandgap values, the CB potentials of these two composites were calculated to be −0.63 eV and −0.94 eV *vs.* NHE, respectively.[30,31] And the corresponding band structures were further depicted as shown in Fig. S5. The thermodynamical photoredox potentials required for the transformations of $O_2/^{\bullet}O_2^-$ and $C_6H_5CH_3/C_6H_5CH_2^{\bullet}$ are −0.33 eV and +1.60 eV *vs.* NHE, respectively. Thus, both CsPCN and CBB were potentially capable of driving the O_2 activation and benzylic C(sp^3)–H bonds oxidation process.[32–36]

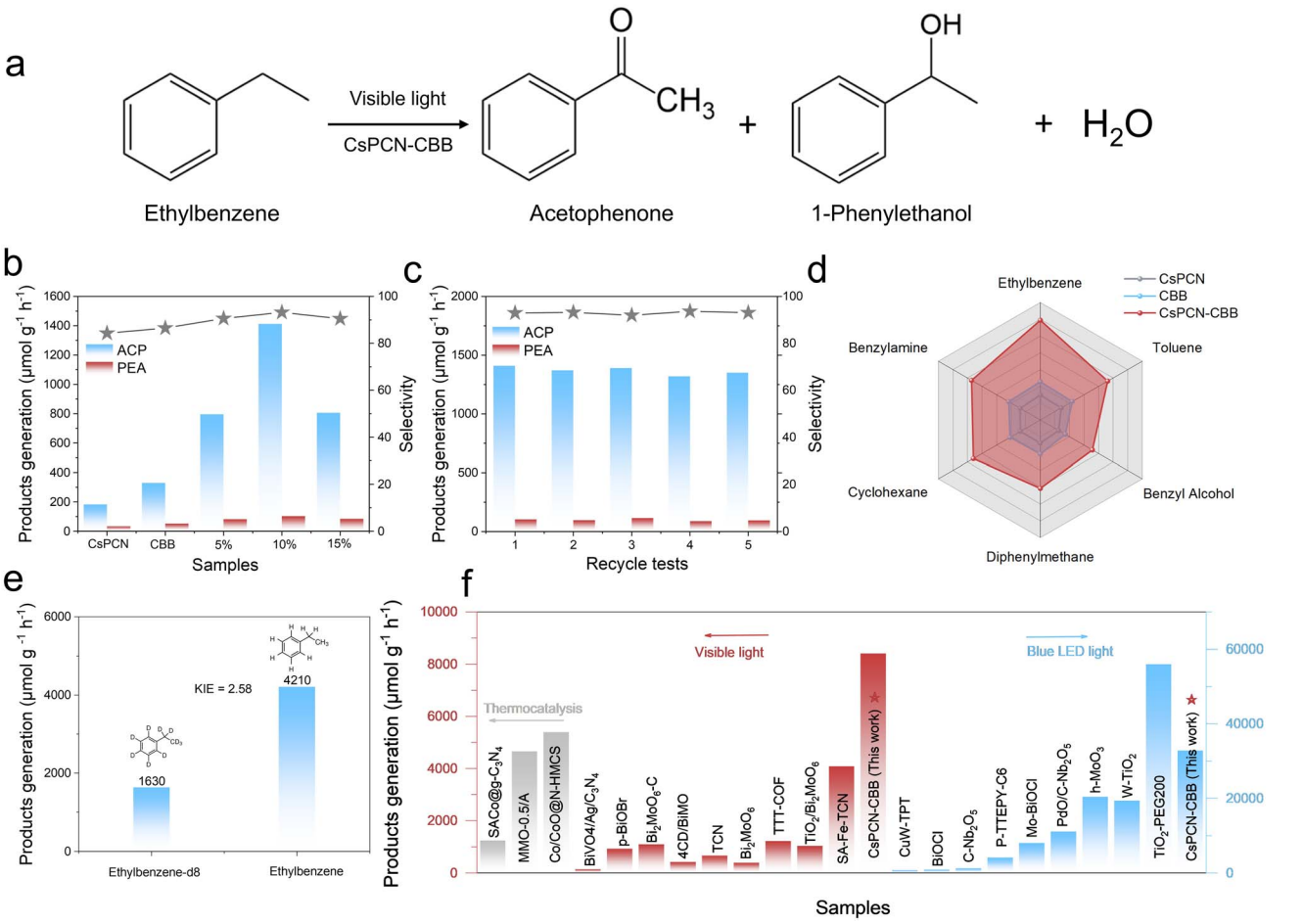

Fig. 2 (a) The scheme of selectively photocatalytic oxidation of ethylbenzene into acetophenone. (b) Photocatalytic activities of blank CBB, CsPCN, *x*% CsPCN–CBB (*x* = 5, 10, 15). (c) Recycle tests over CsPCN–CBB composite. (d) Rader plot of photocatalytic aerobic oxidation reactions with different reactants. (e) Kinetic isotope effect (KIE) experiments of CsPCN–CBB composite. (f) Performance comparison with other photocatalytic or thermocatalytic systems.

With the photocatalytic aerobic oxidation of C(sp^3)–H bond in ethylbenzene as a model reaction, the performances of these synthesized photocatalysts (CBB, CsPCN and CsPCN–CBB) were evaluated in detail. Upon irradiation with visible light ($\lambda > 420$ nm) under oxygen atmosphere conditions (Fig. 2a), ethylbenzene was generally converted to acetophenone (ACP) or 1-phenylethanol (PEA) in a suspension containing 4 mL of acetonitrile, 1 mL of ethylbenzene, and 5 mg of photocatalyst. The experiments for standard curves of the products had been conducted and depicted in Fig. S6. As displayed in Fig. 2b, the blank CBB and CsPCN both showed relatively low activity, possibly owing to the slow charge separation and limited surface reactivity. While the formation of the CsPCN–CBB heterostructure led to a great enhancement in the selective formation of ACP, confirming the necessity of forming heterostructure. The photocatalytic activity of the CsPCN–CBB composites exhibited a volcano-type trend with varying mass ratios. Notably, the 10% CsPCN–CBB heterostructure showed optimal performance, with an ACP yield 4.3-fold higher than that of the blank CBB (Fig. 2b). Additionally, the effects of the light intensity on ACP yield were also studied by changing the multi-channel photoreactors with LED lamp (86 mW cm^{-2}) to the photocatalytic system with xenon lamp (215.8 mW cm^{-2}), where a reaction rate of 42.1 μmol h^{-1} was achieved, displaying a 3-fold enhancement (Fig. S7). To test the recyclability and chemical stability of the 10% CsPCN–CBB composite, cycling stability tests and long-term reaction experiments were performed. As shown in Fig. 2c, the CsPCN–CBB still maintained stable photocatalytic conversion ability after five consecutive recycling tests. Moreover, the CsPCN–CBB composite showed no obvious deactivation of photocatalytic performance during the long-term reaction process under visible light irradiation for 16 h, demonstrating its outstanding stability (Fig. S8). In addition, the photocatalysts used were further collected and tested *via* UV-Vis DRS, XRD, SEM, XPS and FT-IR characterizations (Fig. S9 and S13), no significant degradations were observed as compared to the fresh counterparts, further indicating the stability of the structure. To figure out the universal applicability of the heterostructure, the photocatalytic aerobic oxidation of C(sp^3)–H bond in other organic chemicals were evaluated, such as toluene, benzyl alcohol, cyclohexane, benzylamine and diphenylmethane. As depicted in Fig. 2d and Table S1, the CsPCN–CBB composite exhibited excellent photocatalytic performances compared with the blank CsPCN and CBB, which affirmed that the CsPCN–CBB composite could function as a versatile catalyst for the photocatalytic C(sp^3)–H bond activation. To probe the rate-determining step (RDS) in ethylbenzene oxidation, hydrogen/deuterium kinetic isotope effect (KIE) experiments were carried out (Fig. 2e).[37] Upon replacing ethylbenzene with its deuterated analogue, a pronounced KIE value of 2.58 was obtained, suggesting that the oxidation of C(sp^3)–H (D) bond is likely the RDS in photocatalytic functionalization of hydrocarbons, further demonstrating the significance of C(sp^3)–H bond activation.[38] As illustrated in Fig. 2f and Table S2, the photoactivity of CsPCN–CBB overpassed most of the recently reported photocatalytic systems under different light conditions (visible light and blue LED light), and the apparent quantum yield (AQY) at 420 nm (Fig. S14) is 0.91%, which is comparable to that of other reported photocatalysts, indicating that the CsPCN–CBB is a highly active photocatalyst for C(sp^3)–H bond activation.

The promoted C(sp^3)–H bond activation ability of CsPCN–CBB compared to pristine CsPCN and CBB might be attributed to the formed heterojunction, facilitating charge transfer while preserving strong redox capability, aligning with our initial hypothesis. To reveal the charge transfer mechanism within the CsPCN–CBB composite, X-ray photoelectron spectroscopy (XPS) characterization was first applied to determine the surface chemical states of each element in CsPCN, CBB and CsPCN–CBB composite. As shown in Fig. S15 and S16, the survey and high-resolution spectra confirmed the coexistence of Cs, Bi, Br, C, and N elements in the CsPCN–CBB composite, which was consistent with the results of elemental mapping. Fig. 3a presented high-resolution XPS spectra for Cs species of different samples, where CsPCN showed two peaks with the binding energies of 738.2 and 724.2 eV, corresponding to Cs $3d_{3/2}$ and Cs $3d_{5/2}$, respectively. It could be found that these peaks positively shifted by about 0.1 eV to 738.3 and 724.3 eV, respectively after the formation of CsPCN–CBB. In contrast, negative shifts occurred in Br 3d XPS spectra (Fig. 3b). The broad band at around 69 eV in CBB could be deconvoluted into two peaks at binding energies of 68.3 and 69.3 eV, assigned to Br $3d_{5/2}$ and Br $3d_{3/2}$, respectively. And the peaks of Br $3d_{5/2}$ and Br $3d_{3/2}$ in CsPCN–CBB appeared at 68.2 and 69.2 eV, about 0.1 eV lower than the counterparts of blank CBB. These phenomena solidly indicated the directional transfer of electrons from CsPCN to CBB upon contact, leading to Fermi level equilibrium and the establishment of an interfacial electric field (IEF) directed from CsPCN to CBB. The formed IEF may provide a driving force to steer the photoexcited electron transfer from CBB to CsPCN under illumination. For a more comprehensive understanding of the flow of photoexcited electrons within the composites, *in situ* XPS was conducted. As shown in Fig. 3c and S17, the peaks of Bi 4f, Br 3d of CsPCN–CBB moved to higher energy levels after light illumination; while the binding energies of those peaks that were ascribed to cyano group in C 1s and C–N=C in N 1s obviously shifted to lower energy levels, confirming the transfer direction of photogenerated electrons from CBB to CsPCN under light irradiation.[39,40] To further convince the charge transfer pathways, density functional theory (DFT) simulations were performed to determine the work functions of CsPCN and CBB. CBB displayed a larger work function (6.20 eV) compared to CsPCN (3.03 eV), suggesting that charge migration from CsPCN to CBB could occur spontaneously upon contact in the dark to reach Fermi level equilibrium (Fig. S18 and S19). This charge redistribution would induce an interfacial electric field directed from CsPCN to CBB, consistent with XPS analysis. The formation of such electric field would drive the photoexcited electrons in the conduction band of CBB migrating toward the valence band of CsPCN under light irradiation and recombining with holes there.

To further figure out how the charge transfer pathway in the heterostructure affected the charge dynamics in the photocatalytic system, temperature-dependent photoluminescence

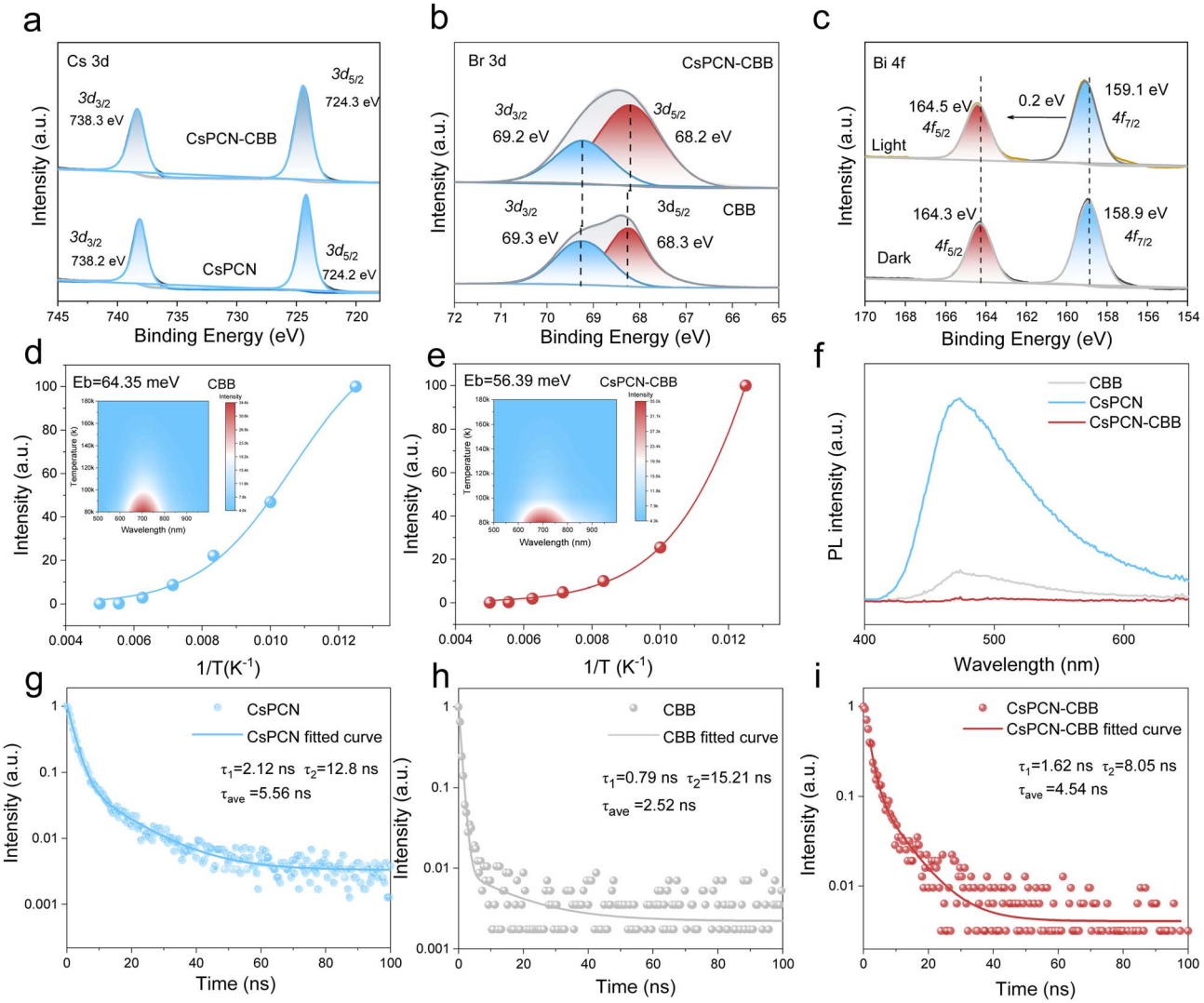

Fig. 3 High-resolution XPS spectra of (a) Cs 3d, (b) Br 3d core levels of CBB, CsPCN and CsPCN–CBB composites. *In situ* XPS spectra of Bi 4f (c) in CsPCN–CBB composites. (d and e) Temperature-dependent photoluminescence of CBB and CsPCN–CBB. (f) Steady-state PL spectra, and (g–i) time-resolved PL decay spectra for CsPCN, CBB and CsPCN–CBB.

spectroscopy was employed to assess the changes in exciton binding energy. The PL emission intensity exhibited progressive quenching with increasing temperature from 80 to 180 K (Fig. 3d, e and S20), indicative of thermally activated non-radiative recombination pathways. Quantitative analyses revealed a substantially reduced exciton binding energy of 56.39 meV for CsPCN–CBB relative to blank CsPCN (76.68 meV) and CBB (64.35 meV). This reduction implied enhanced dissociation efficiency of excitons into free charge carriers and accelerated charge transfer kinetics in CsPCN–CBB, which would facilitate more photogenerated charge carriers to participate in the photocatalytic reactions.[41] As displayed in Fig. S21a, CsPCN–CBB indeed displayed the strongest photocurrent density compared to blank CBB and CsPCN, ascribed to the quicker charge transfer and separation rate after constructing the heterojunction. Similar performance was obtained in the electrochemical impedance spectroscopy (EIS) spectra.[42] CsPCN–CBB presented the minimum radius, suggesting that CsPCN–CBB had the fastest charge transfer rate and the lowest recombination ability (Fig. S21b). Further, open-circuit potential (OCPT) measurements were used to investigate the formation of the internal electric field (IEF) and its effect on photogenerated charge behavior (Fig. S21c). Compared to blank CBB and CsPCN, the CsPCN–CBB composite exhibited the highest ΔOCPT ($OCPT_{dark}$–$OCPT_{light}$), suggesting that the heterostructure provided an intrinsic built-in electric field to facilitate charge transfer. Moreover, steady-state photoluminescence (PL) measurements were utilized to characterize the three samples with an excitation wavelength at 340 nm. As displayed in Fig. 3f, a weaker PL emission intensity was observed in the CsPCN–CBB sample than that of blank CBB and CsPCN, which indicated that the CsPCN–CBB possessed excellent efficiency in separating photogenerated electron–hole pairs, highly possibly owing to the formation of the

heterostructure. This was further corroborated by time-resolved PL (TRPL) decay measurements (Fig. 3g–i), where the dynamics were fitted with a decay model consisting of two consecutive mono-exponential components. Before the formation of heterostructure, CBB possessed an average luminescence decay lifetime of 2.52 ns, which was greatly affected by the introduction of CsPCN. Upon formation of heterostructure, the CsPCN–CBB exhibited a much longer average lifetime of 4.54 ns, demonstrating that the formation of heterostructure could effectively inhibit the recombination of photogenerated carriers and enhance the transport and utilization of photogenerated carriers. These findings collectively convinced the crucial role of the heterojunction in promoting charge separation and prolonging carrier lifetimes, ultimately enhancing photocatalytic C(sp^3)–H bond activation ability.

To understand how the formed heterostructure effectively activated the C(sp^3)–H bond, the room-temperature *in situ* electron paramagnetic resonance (EPR) measurements were first conducted to probe the active species and intermediates formed during the photocatalytic oxidation process, where dimethyl pyridine *N*-oxide (DMPO) was selected as the trapping agents. As shown in Fig. S22, no free-radical signals were detected in the dark. However, under visible light irradiation, six characteristic signal peaks were observed, belonging to the DMPO-Cα radical adduct (α_H = 23.1 and α_N = 14.7, corresponding to the hydrogen and nitrogen hyperfine splittings of the nitroxide nitrogen). And the radical signals over CsPCN–CBB were more significant than those of blank CBB and CsPCN, which was in agreement with the photocatalytic performance, indicating that a larger amount of such Cα radicals could be photogenerated in a CsPCN–CBB-catalyzed system (Fig. 4a).[43,44] Furthermore, the intensities of the DMPO-Cα radical peaks continuously increased with the radiation time, indicating the continuous formation of carbon-centered radicals during the photocatalytic reaction (Fig. 4b). Moreover, the reactive oxygen species generated during the photocatalytic reaction process has also been tested. The result confirmed no generation of $^{\bullet}OH$ but the clear appearance of $^{\bullet}O_2^-$ signal in the photocatalytic ethylbenzene oxidation process (Fig. S23). Especially, the EPR signals of $^{\bullet}O_2^-$ radical produced by CsPCN–CBB were significantly enhanced compared with that of blank CBB and CsPCN, demonstrating the $^{\bullet}O_2^-$ involved reaction pathway and an enhanced O_2 activation ability by photogenerated electrons in the CsPCN–CBB composite.[45] Then, scavenger studies as well as control experiments were conducted to further explore the reaction mechanisms (Fig. 4c). No products were observed under dark conditions, suggesting that the presence of light was crucial for the reaction. When the reaction atmosphere was switched from oxygen to air or argon, a significant decrease in photoactivity was observed, further proving that oxygen played a crucial role in this reaction. The introduction of *p*-benzoquinone (*p*-BQ) as a superoxide radical scavenger resulted in a sharp decline in catalytic performance, solidly demonstrating the free-radical $^{\bullet}O_2^-$ based reaction pathway. The addition of $AgNO_3$ or methyl alcohol (MeOH) as scavengers for photogenerated electrons (e^-) or holes (h^+) reduced the reactivity, highlighting the significance of concurrent involvement of both photogenerated electrons and holes in the process. To gain deeper insight into the photocatalytic ethylbenzene oxidation reaction process, *in situ* diffuse reflectance infrared Fourier transform spectroscopy (DRIFTS) measurements were conducted to identify the intermediates and products formed during the reaction. Ethylbenzene was first introduced to the surface of photocatalysts to reach an adsorption–desorption equilibrium state *via* continuous flow of ethylbenzene vapor. It can be found from Fig. 4d that CsPCN–CBB exhibited excellent ethylbenzene adsorption peaks, demonstrating a greater ethylbenzene adsorption capacity. Upon light irradiation and oxygen introduction, those characteristic peaks of ethylbenzene at 1604, 1496, and 1453 cm^{-1} (C=C stretching vibration of phenyl group) gradually weakened, demonstrating a rapid consumption of ethylbenzene. In contrast, new peaks at ~1697 cm^{-1} ascribed to C=O of acetophenone appeared and gradually increased in intensity with time, indicating the photocatalytic generation and accumulation of acetophenone. The blue shifts of the bending mode of CH_3 (1376 cm^{-1}) in ethylbenzene to 1358 cm^{-1} further convinced the photocatalytic aerobic oxidation of ethylbenzene.[46,47] In contrast, the blank CBB revealed relatively less pronounced attenuation of benzene ring vibrations and slower C=O bond formation kinetics (Fig. S24). To further elucidate the correlation between catalyst structure and photocatalytic C(sp^3)–H bond oxidation performance, theoretical calculations were conducted to investigate the adsorption and activation of O_2 and ethylbenzene on different catalysts (Fig. 4e, f and S25). As shown in Fig. 4e, owing to the outstanding adsorption affinity of CsPCN toward oxygen as compared with the blank CBB, the incorporation of CsPCN to CBB markedly promoted the adsorption of oxygen on the surface of CsPCN–CBB heterostructure. This enhancement of oxygen adsorption would facilitate the formation of $^{\bullet}O_2^-$ for photocatalytic oxidation of C(sp^3)–H bond by reducing the adsorbed oxygen with photogenerated electrons. Moreover, the ethylbenzene adsorption experiment of the catalysts is presented in Fig. S26, the blank CsPCN demonstrates the highest adsorption amount of ethylbenzene, while the CsPCN–CBB heterojunction exhibits greater ethylbenzene adsorption than blank CBB. The finding validates that the introduction of CsPCN benefits ethylbenzene adsorption, which is consistent with the results obtained from theoretical calculations. In addition, it can be found from the calculated relative Gibbs free energies (Fig. 4f, S27 and S28), as for CBB, the primary energy barrier for C(sp^3)–H oxidation pathway is the adsorption of ethylbenzene. While this thermodynamic barrier can be significantly reduced by introducing CsPCN into CBB, thereby enabling the formed CsPCN–CBB heterostructure with accelerated conversion performance of ethylbenzene into acetophenone. These theoretical insights, in concert with experimental evidence collectively and unambiguously substantiated that the rational design of CsPCN–CBB heterostructure could not only optimize interfacial charge redistribution but also tailor surface reaction energetics, thus resulting in superior photocatalytic performance.

Based on aforementioned discussions, a reaction mechanism of photocatalytic oxidation of ethylbenzene by CsPCN–

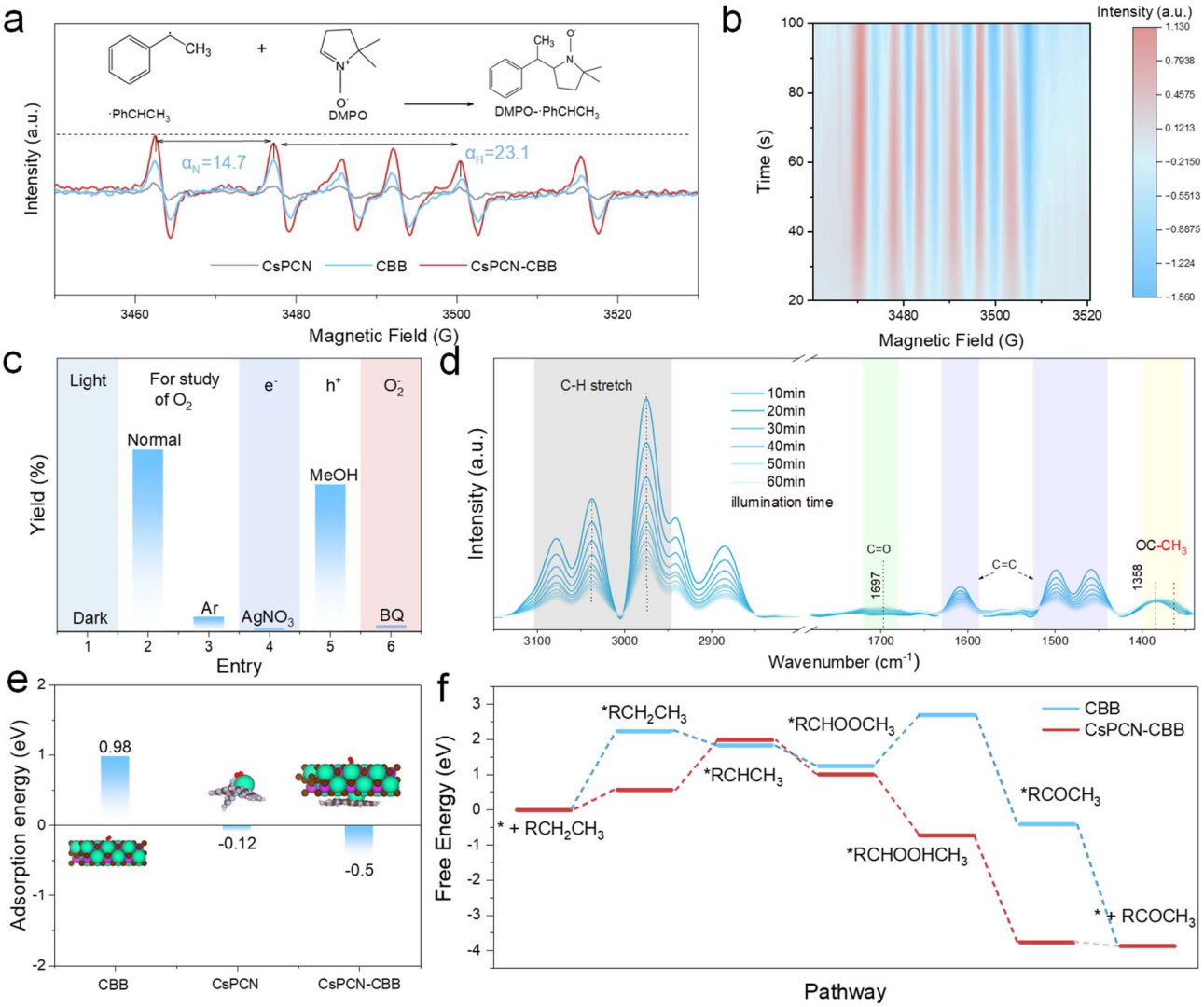

Fig. 4 (a) The comparison of EPR spectra of different composites under light irradiation. (b) Time dependent *in situ* EPR spectra of the generated DMPO-Cα radical within the CsPCN–CBB system upon irradiation. (c) Control experiments of photocatalytic ethylbenzene oxidation under different conditions. (d) Time dependent *in situ* DRIFT spectra of CsPCN–CBB under ethylbenzene and O_2 atmosphere under irradiation. (e) Adsorption energy of oxygen on CBB, CsPCN and CsPCN–CBB. (f) Relative Gibbs free energy diagrams of photocatalytic ethylbenzene oxidation over CsPCN and CsPCN–CBB composite.

CBB was proposed in Fig. S29–S30. Under light illumination, the charge carriers were excited simultaneously in both CsPCN and CBB. Due to the formation of an internal electric field at the contact interface between the two components, the photogenerated electrons in the CB of CBB combine with the h^+ in the VB of CsPCN. Thus, the photogenerated holes accumulated at the VB of CBB, while electrons accumulated at the CB of CsPCN. Subsequently, the photogenerated holes activated the C(sp^3)–H bond in ethylbenzene to form carbon-centered radicals (R–$^{\cdot}CHCH_3$), while the photogenerated electrons were captured by O_2 to produce $^{\cdot}O_2^-$. The majority of the $CHCH_3^{\cdot}$ reacted with $^{\cdot}O_2^-$ and proton concertedly to generate acetophenone instantly by eliminating a water molecule. At the same time, minority $CHCH_3^{\cdot}$ would react with O_2 to generate 1-phenylethanol. Overall, the formation of the CsPCN–CBB heterojunction significantly enhanced the separation and utilization efficiency of the photogenerated carriers, thereby enabling an excellent photocatalytic performance toward C(sp^3)–H bond oxidation.

3 Conclusions

In summary, we successfully constructed a CsPCN–CBB heterojunction *via* an *in situ* anti-solvent method, which exhibited remarkable efficiency in photocatalytic C(sp^3)–H bond activation under visible light irradiation. Spectroscopic analyses combined with density functional theory calculations demonstrated that the well-defined heterointerface promoted the directional charge transfer pathway and facilitated the adsorption of oxygen and ethylbenzene. The synergistic effect not only enhanced charge separation, but also enriched reactant molecules at the catalytic interface. Additionally, the formation of heterojunction lowered the free-energy barriers of

the oxidation pathway, thus ultimately delivering substantially improved ethylbenzene oxidation activity compared with the single components. Beyond highlighting the feasibility of all-inorganic lead-free perovskite-based heterostructures for selective organic transformations, this work also illustrates the broader potential of heterojunction engineering as a powerful strategy to couple charge dynamics with interfacial reactivity, thereby opening new avenues for the rational design of high-performance photocatalysts in sustainable organic synthesis.

Author contributions

Taoran Chen and Yu Han: data curation, formal analysis, validation, writing – original draft. Guojin Huang and Zhengwu Liao: data curation, formal analysis, resources. Ying Tao: theoretical calculation; Yue Zheng: temperature-dependent continuous photoluminescence spectroscopy test, Yu Wang: PL and TRPL measurements, Wei Zhao, Shiqi Li: XPS and *in situ* XPS tests. YuLin Wang: conceptualization, formal analysis. Hongli Sun and Chenliang Su: data curation, formal analysis, funding acquisition, investigation, supervision, writing – original draft, writing – review & editing.

Conflicts of interest

The authors declare no conflict of interest.

Data availability

The data that support the findings of this study are available within the article and supplementary information (SI). Supplementary information is available. See DOI: https://doi.org/10.1039/d5sc09692h.

Acknowledgements

This work was supported by the National Key Research and Development Program of China (2021YFA1600800), National Natural Science Foundation of China (22102102, 22372102), Shenzhen Science and Technology Program (20231122120657001, RCJC20200714114434408), Research Team Cultivation Program of Shenzhen University (2023QNT013), Scientific Foundation for Youth Scholars of Shenzhen University (868-000001032185), Shenzhen Peacock Plan (20210308299C), Science and Technology Innovation Commission of Shenzhen (ZDSYS201707271014468), China Postdoctoral Science Foundation (2023M742395).

References

1 H. Huang, H. Yuan, J. Zhao, G. Solís-Fernández, C. Zhou, J. W. Seo, J. Hendrix, E. Debroye, J. A. Steele, J. Hofkens, J. Long and M. B. J. Roeffaers, *ACS Energy Lett.*, 2019, **4**, 203–208.
2 G. Zhou, B. Lei and F. Dong, *ACS Catal.*, 2024, **14**, 4791–4798.
3 X. Xiao, Z. Ruan, Q. Li, L. Zhang, H. Meng, Q. Zhang, H. Bao, B. Jiang, J. Zhou, C. Guo, X. Wang and H. Fu, *Adv. Mater.*, 2022, **34**, 2200612.
4 H. Wang, C. Cao, D. Li, Y. Ge, R. Chen, R. Song, W. Gao, X. Wang, X. Deng, H. Zhang, B. Ye, Z. Li and C. Li, *J. Am. Chem. Soc.*, 2023, **145**, 16852–16861.
5 Y. Tao, J. Ding, Z. Teng, Q. Xu, W. Ou, H. Sun, S. Li, L. Yu, G. Li, B. Liu and C. Su, *J. Am. Chem. Soc.*, 2025, **147**, 18814–18825.
6 W. Zhang, G. E. Eperon and H. J. Snaith, *Nat. Energy*, 2016, **1**, 16048.
7 J. Chen, C. Dong, H. Idriss, O. F. Mohammed and O. M. Bakr, *Adv. Energy Mater.*, 2020, **10**, 1902433.
8 T. Chen, T. Qin, H. Sun and C. Su, *Rare Met.*, 2025, **44**, 6354–6365.
9 W. Xiang and W. Tress, *Adv. Mater.*, 2019, **31**, 1902851.
10 H. Mai, D. Chen, Y. Tachibana, H. Suzuki, R. Abe and R. A. Caruso, *Chem. Soc. Rev.*, 2021, **50**, 13692–13729.
11 F. Xu, K. Meng, B. Cheng, S. Wang, J. Xu and J. Yu, *Nat. Commun.*, 2020, **11**, 4613.
12 R. Gao, R. Shen, C. Huang, K. Huang, G. Liang, P. Zhang and X. Li, *Angew. Chem., Int. Ed.*, 2025, **64**, e202414229.
13 G. dos Santos, L. Tian, R. Gonçalves, H. García and L. Rossi, *Adv. Funct. Mater.*, 2025, **35**, 2422055.
14 J. Fu, J. Yu, C. Jiang and B. Cheng, *Adv. Energy Mater.*, 2018, **8**, 1701503.
15 S. Patnaik, D. P. Sahoo and K. Parida, *Carbon*, 2021, **172**, 682–711.
16 J. Jiang, L. Yu, J. Peng, W. Gong and W. Sun, *Carbon Lett.*, 2025, **35**, 417–440.
17 X. Fang, B. Li, J. Huang, C. Hu, X. Yang, P. Feng, X. Dong, J. Wu, Y. Li and Y. Ding, *Energy Environ. Sci.*, 2025, **18**, 6202–6213.
18 L. Luo, Q. Wu, S. Wang, H. Song, J. Li, L. Zhang, Q. Zhang, Y. Fang, B. Jiang and X. Wang, *Angew. Chem., Int. Ed.*, 2025, **64**, e202507415.
19 Z. Teng, Z. Zhang, Y. Tu, Q. Zhang, N. Jian, L. Yang, J. Xiao, J. Ding, L. Huang, O. Teruhsia, C. Wang, D. Zhang, H. Yu, J. Lu, C. Su and B. Liu, *Nat. Nanotechnol.*, 2025, **20**, 815–824.
20 T. Chen, M. Li, L. Shen, M. B. J. Roeffaers, B. Weng, H. Zhu, Z. Chen, D. Yu, X. Pan, M.-Q. Yang and Q. Qian, *Front. Chem.*, 2022, **10**, 833784.
21 L. Shen, H. Kang, L. Deng, Z. Chen and M.-Q. Yang, *J. Catal.*, 2024, **434**, 115499.
22 B. Su, S. Wang, W. Xing, K. Liu, S.-F. Hung, X. Chen, Y. Fang, G. Zhang, H. Zhang and X. Wang, *Angew. Chem., Int. Ed.*, 2025, **64**, e202505453.
23 X. Zhang, P. Ma, C. Wang, L. Gan, X. Chen, P. Zhang, Y. Wang, H. Li, L. Wang, X. Zhou and K. Zheng, *Energy Environ. Sci.*, 2022, **15**, 830–842.
24 X. Zhang, H. Su, P. Cui, Y. Cao, Z. Teng, Q. Zhang, Y. Wang, Y. Feng, R. Feng, J. Hou, X. Zhou, P. Ma, H. Hu, K. Wang, C. Wang, L. Gan, Y. Zhao, Q. Liu, T. Zhang and K. Zheng, *Nat. Commun.*, 2023, **14**, 7115.
25 N. V, G. N. Nagy, A. Rahaman, S. K. Kalpathy, T. Thomas, S. T. P and M. U. Kahaly, *Mater. Adv.*, 2024, **5**, 6426–6439.

26 X. Liao, X. Jia, W. Li, X. Lang, J. Zhang, X. Zhao, Y. Ji, Q. Du, C.-H. Kuan, Z. Ren, W. Huang, Y. Bai, K. Zhang, C. Xiao, Q. Lin, Y.-B. Cheng and J. Tong, *Nat. Commun.*, 2025, **16**, 1164.
27 Z.-J. Bai, Y. Mao, B.-H. Wang, L. Chen, S. Tian, B. Hu, Y.-J. Li, C.-T. Au and S.-F. Yin, *Nano Res.*, 2023, **16**, 6104–6112.
28 Z.-J. Bai, S. Tian, T.-Q. Zeng, L. Chen, B.-H. Wang, B. Hu, X. Wang, W. Zhou, J.-B. Pan, S. Shen, J.-K. Guo, T.-L. Xie, Y.-J. Li, C.-T. Au and S.-F. Yin, *ACS Catal.*, 2022, **12**, 15157–15167.
29 B. Lei, J. Sheng, F. Zhong, C. Du, Y. He, J. Li and F. Dong, *J. Catal.*, 2024, **429**, 115270.
30 C. Liu, X. Ren, S. R. Sahoo, A. Kuklin, C. Yao, H. Ågren and Y. Zhang, *Adv. Sci.*, 2025, e12163.
31 X. Wu, W. Zhao, Y. Hu, G. Xiao, H. Ni, S. Ikeda, Y. Ng and F. Jiang, *Adv. Sci.*, 2022, **9**, 2204029.
32 Y. Nosaka and A. Y. Nosaka, *Chem. Rev.*, 2017, **117**, 11302–11336.
33 C. Bie, L. Wang and J. Yu, *Chem*, 2022, **8**, 1567–1574.
34 L. Luo, T. Zhang, M. Wang, R. Yun and X. Xiang, *ChemSusChem*, 2020, **13**, 5173–5184.
35 C. Chen, M. Wu, B. Chen, C. Ma, M. Song and G. Jiang, *Proc. Natl. Acad. Sci. U. S. A.*, 2023, **120**, e2310004120.
36 Y.-F. Ding, S.-F. Yin and M.-Q. Cai, *J. Colloid Interface Sci.*, 2023, **630**, 452–459.
37 S. Kopf, F. Bourriquen, W. Li, H. Neumann, K. Junge and M. Beller, *Chem. Rev.*, 2022, **122**, 6634–6718.
38 L. Luo, Y.-Q. Zhu, W. Chen, Y. Miao, S. Zhang, Y. Yang, Z. Li and M. Shao, *Angew. Chem., Int. Ed.*, 2025, **64**, e202505544.
39 L. Wang, B. Cheng, L. Zhang and J. Yu, *Small*, 2021, **17**, 2103447.
40 J. Ma, L. Xu, Z. Yin, Z. Li, Z. Song, J. Qiu and Y. Li, *Green Energy Environ.*, 2025, **10**, 1073–1084.
41 T. Zhang, C. Zhou, X. Feng, N. Dong, H. Chen, X. Chen, L. Zhang, J. Lin and J. Wang, *Nat. Commun.*, 2022, **13**, 60.
42 Y. Tao, Z. Ma, W. Wang, C. Zhang, L. Fu, Q. Zhu, Y. Li, G. Li and D. Zhang, *Adv. Funct. Mater.*, 2023, **33**, 2211169.
43 T. Chen, B. Weng, S. Lu, H. Zhu, Z. Chen, L. Shen, M. B. J. Roeffaers and M.-Q. Yang, *J. Phys. Chem. Lett.*, 2022, **13**, 6559–6565.
44 M.-H. Sun, M.-Y. Qi, C.-L. Tan, Z.-R. Tang and Y.-J. Xu, *Chin. Chem. Lett.*, 2023, **34**, 108022.
45 Y.-X. Tan, Z.-M. Chai, B.-H. Wang, S. Tian, X.-X. Deng, Z.-J. Bai, L. Chen, S. Shen, J.-K. Guo, M.-Q. Cai, C.-T. Au and S.-F. Yin, *ACS Catal.*, 2021, **11**, 2492–2503.
46 M. Chen, N. Maeda, A. Baiker and J. Huang, *ACS Catal.*, 2018, **8**, 6594–6600.
47 Y. Shi, P. Li, H. Chen, Z. Wang, Y. Song, Y. Tang, S. Lin, Z. Yu, L. Wu, J. C. Yu and X. Fu, *Nat. Commun.*, 2024, **15**, 4641.